Dalton Transactions

PAPER

View Article Online
View Journal | View Issue



Cite this: *Dalton Trans.*, 2015, **44**, 8126

# Structure and properties of binder gels formed in the system $Mg(OH)_2$–$SiO_2$–$H_2O$ for immobilisation of Magnox sludge

Sam A. Walling,[a] Hajime Kinoshita,[a] Susan A. Bernal,[a] Nick C. Collier[a,b] and John L. Provis*[a]

A cementitious system for the immobilisation of magnesium rich Magnox sludge was produced by blending an $Mg(OH)_2$ slurry with silica fume and an inorganic phosphate dispersant. The $Mg(OH)_2$ was fully consumed after 28 days of curing, producing a disordered magnesium silicate hydrate (M–S–H) with cementitious properties. The structural characterisation of this M–S–H phase by $^{29}Si$ and $^{25}Mg$ MAS NMR showed clearly that it has strong nanostructural similarities to a disordered form of lizardite, and does not take on the talc-like structure as has been proposed in the past for M–S–H gels. The addition of sodium hexametaphosphate $(NaPO_3)_6$ as a dispersant enabled the material to be produced at a much lower water/solids ratio, while still maintaining the fluidity which is essential in practical applications, and producing a solid monolith. Significant retardation of M–S–H formation was observed with larger additions of phosphate, however the use of 1 wt% $(NaPO_3)_6$ was beneficial in increasing fluidity without a deleterious effect on M–S–H formation. This work has demonstrated the feasibility of using M–S–H as binder to structurally immobilise Magnox sludge, enabling the conversion of a waste into a cementitious binder with potentially very high waste loadings, and providing the first detailed nanostructural description of the material thus formed.

Received 3rd March 2015,
Accepted 25th March 2015

DOI: 10.1039/c5dt00877h

www.rsc.org/dalton

## 1. Introduction

The United Kingdom has operated a fleet of Magnox nuclear power plants for over 50 years, utilising natural uranium fuel clad in an Mg–Al alloy (Magnox) casing. Corrosion of this cladding during reprocessing and storage has resulted in the accumulation of a substantial quantity of legacy $Mg(OH)_2$-rich sludges in storage ponds and silos. In 2013 it was estimated that there were 1497 $m^3$ of sludge in the Magnox Fuel Storage Pond alone,[1] mainly constituting $Mg(OH)_2$ with some corroded uranium, hydrotalcite ($Mg_6Al_2(CO_3)(OH)_{16}{\cdot}4H_2O$),[2] and artinite ($Mg_2CO_3(OH)_2{\cdot}3H_2O$),[3] along with a significant quantity of mixed radionuclides including $^{90}Sr$, $^{137}Cs$, $^{241}Am$ and isotopes of Pu.[4] In the UK these sludges are classified as Intermediate Level Wastes (ILW), that is, significantly radioactive but not heat generating,[2] and thus treatment is required for their safe immobilisation and disposal.

Portland Cement (PC) composites blended with high quantities of supplementary cementitious materials such as blast furnace slag (BFS) and fly ash (FA) have long been the preferred matrices for the encapsulation of much of the ILW inventory in the United Kingdom.[5] A recent study by Collier and Milestone[6] reported that no significant chemical interaction occurred between $Mg(OH)_2$ sludge and FA:PC and BFS:PC cement matrices, with no identifiable incorporation of magnesium into the hydrated binder products. This indicated that the solids of the sludge were encapsulated in the matrix, rather than chemically bound. The use of PC-based materials may not be optimal for Magnox sludge immobilisation/encapsulation as the variable water content of the sludges can cause issues related to the release of bleed water when blended with conventional encapsulation grouts.[7] The conventional PC-based grouts also occupy a significant space as a matrix to encapsulate the waste, limiting the physical space for waste loading possible per package. The development of a tailored binder, which uses the sludge as the basis for a cementitious matrix, could enable higher waste loadings to be achieved, and could also reduce the footprint of the encapsulated waste in a future geological disposal facility (GDF).

Alternative binders such as magnesium-based cements have been studied in recent years as part of the push towards

[a]*Immobilisation Science Laboratory, Department of Materials Science & Engineering, The University of Sheffield, Sheffield, S1 3JD, UK. E-mail: j.provis@sheffield.ac.uk; Tel: +44 (0)114 222 5490*
[b]*National Nuclear Laboratory, Chadwick House, Warrington Road, Birchwood Park, Warrington, WA3 6AE, UK*

reducing the environmental footprint associated with the production of Portland cement materials, and the development of sustainable fit-for purpose alternative cements.[8] This largely stems from the ability to calcine magnesite ($MgCO_3$) to form magnesia (MgO) at a lower temperature than is required for the conversion of calcite ($CaCO_3$) to PC, leading to potential energy savings.[9] Magnesium-based cements are often produced by combining MgO with phosphates or magnesium chlorides, to form magnesium phosphate cements (also known as chemically bonded phosphate ceramics or acid–base cements)[10] or magnesium oxychloride cement,[11] respectively. However, in the last decade magnesium silicate hydrate (M–S–H) cements based on blends of MgO and silica fume have attracted attention as binders in refractory castables, and as lower pH cements for the immobilisation of ILW containing reactive metals, which would corrode and generate hydrogen if encapsulated in PC-based materials.[12]

The $MgO–SiO_2–H_2O$ system has been the subject of studies to determine the reaction products formed from solution, both under hydrothermal[13] and low temperature[14] conditions, with a combination of both talc and serpentine-like phases identified among the reaction products. Studies have increasingly focussed on the potential for M–S–H as a cement, using dead burnt MgO–silica fume (SF) blends at ambient temperatures,[15] light burnt MgO–SF blends,[12a] and $MgO–MgCO_3$–SF-quartz sand composites.[12c] However, work based on the use of $Mg(OH)_2$ as the main Mg source has not been as prominent, and the formation of M–S–H type gels within the $Mg(OH)_2$–SF–$H_2O$ system cured at near-ambient temperatures has not been studied for cementing applications.

The formation of poorly crystalline M–S–H gels has also been identified in conventional Portland cements after exposure to sulfate attack,[16] and it has been postulated that M–S–H forms as a secondary product in BFS:PC blended cements.[17] Recent studies have also identified M–S–H as an alkaline-alteration product of nuclear waste glasses,[18] and as a phase formed in low-pH cements as a result of interactions with groundwater under nuclear waste repository conditions.[19] The identification of such phases in these key environments related to nuclear waste disposal highlights the importance of developing a full structural characterisation of the M–S–H gel, which remains poorly understood at present.

In this study hydrated $Mg(OH)_2$:SF blends are produced and characterised up to 28 days of curing, with a focus on assessing workability, strength, phase development and gel structure of the M–S–H system. Due to industry and regulatory concerns about the possibility of organic superplasticisers enhancing radionuclide solubility within nuclear wasteform cements,[20] the application of an inorganic deflocculant (sodium hexametaphosphate $(NaPO_3)_6$), as used in castables and for clay dispersions[21] was also investigated as a means to reduce water demand. This additive has previously been used in M–S–H cements,[12a,15a] but its effect on fluidity and phase formation within these cements has not yet been described in detail.

# 2. Experimental methodology

## 2.1 Materials

The raw materials used were $Mg(OH)_2$ from Intermag Company Ltd (<95% purity), silica fume (SF) 181 (Microsilica 940-U, >90% $SiO_2$) supplied by Elkem as an undensified dry powder, and sodium hexametaphosphate ($(NaPO_3)_6$, 65–70% $P_2O_5$ basis) supplied by Sigma-Aldrich.

## 2.2 Formulation design

Throughout the experiments, a mix design of 1 : 1 $Mg(OH)_2$ : SF was utilised. The influence of the $(NaPO_3)_6$ in the range 0 to 5 wt% of the binder, and the water/binder (w/b) ratio, on the workability of the M–S–H system was investigated *via* mini-slump testing, as described in section 2.4. An initial w/b ratio of 1.2 (defined on a mass basis) was tested at different $(NaPO_3)_6$ levels, and then this was systematically reduced by 0.1 unit increments until the samples were no longer fluid (*i.e.* a mini-slump value of 11.3 $cm^2$, corresponding to the base area of the cone), to identify the lowest w/b ratio at which the samples could reasonably be mixed and emplaced. For the system without $(NaPO_3)_6$ the w/b ratio was also increased systematically by 0.1 unit increments from 1.2 due to the low mini-slump values recorded, until a value of ~80 $cm^2$ was achieved. Once an optimal level of phosphate addition was identified, the structural development of this paste was then studied over the time of curing.

## 2.3 Mix methodology

To prepare pastes, $(NaPO_3)_6$ was fully dissolved in distilled water, then $Mg(OH)_2$ was gradually added over 1 minute, and this suspension was mechanically mixed for 3 minutes before adding the silica fume. Mixing continued for an additional 5 minutes, and pastes were then poured into 50 mL centrifuge tubes, sealed, placed in an environmental chamber at 40 °C and 95% relative humidity, and cured for up to 28 days. Preliminary studies showed slow reaction at 20 °C, and therefore an elevated curing temperature of 40 °C was selected.

## 2.4 Analytical methods

Mini-slump testing was performed using a poly(tetrafluoroethene) mini-slump cone (downscaled Abrams cone geometry: 19 mm top diameter, 38 mm bottom diameter, 57 mm height[22]) on a sheet of poly(methyl methacrylate) marked with grid squares of 2 × 2 cm. Freshly mixed pastes were used in triplicate tests, and in each instance a photograph was taken of the final slump from above, from which the slump area was calculated using ImageJ software[23] calibrated to the grid.

For compressive strength testing, the paste was poured into 50 mm steel cube moulds, compacted with the use of a vibrating table, sealed and cured as described above. Cubes were demoulded after 3 days and returned to the environmental chamber. Testing was performed in duplicate using a CONTROLS Automax 5 instrument at a loading rate of 0.25 MPa $s^{-1}$.

Hardened samples which had been cured for 7, 14 and 28 days were crushed and immersed in acetone for 2 days to

arrest hydration, then dried in a vacuum desiccator for a further 2 days. These were then ground with an agate mortar and sieved to <63 μm using a brass sieve for analysis by the following apparatus.

X-ray diffraction (XRD) was carried out using a STOE STADI P diffractometer (Cu Kα, 1.5418 Å) using an imaging plate detector (IP-PSD) to collect data between $10° < 2\theta \leq 70°$, and angle-corrected using a silicon standard. Selected samples were analysed *via* thermogravimetric analysis (TGA) using a Pyris 1 TGA and differential thermal analysis (DTA) using a Perkin Elmer DTA 7, both using an alumina crucible, at a heating rate of 10 °C $min^{-1}$ up to 1000 °C in a nitrogen atmosphere. FTIR spectroscopy was undertaken using a Perkin Elmer Spectrum 2000 spectrometer in mid-IR mode using pressed KBr discs containing 2 wt% powdered sample. Solid state $^{29}Si$ NMR spectra were collected on a Varian VNMRS 400 (9.4 T) using a 6 mm o.d. zirconia rotor. Chemical shifts were externally referenced to tetramethylsilane (TMS) at 0 ppm. $^{29}Si$ MAS NMR spectra for M–S–H were collected at 79.435 MHz, with a spinning speed of 6.8 kHz, a pulse duration of 6.2 μs (90°) and a relaxation time of 30 s, for a minimum of 2000 scans. M–S–H samples for NMR analysis were produced using analytical grade $Mg(OH)_2$ (Alfa Aesar, 95–100% purity) to eliminate any possibility of Fe contamination. $^{29}Si$ MAS NMR spectra for mineral samples (lizardite and antigorite) were collected at 79.438 MHz, with a spinning speed of 6 kHz, a pulse duration of 4.5 μs (90°) and relaxation time of 1 s for 43 200 scans.

$^{25}Mg$ MAS NMR spectra were obtained on a Bruker Avance III 850 spectrometer (19.96 T), using a 4 mm zirconia rotor, with a spinning speed of 10 kHz (M–S–H, lizardite and talc) and 14 kHz (antigorite – required due to signal broadening from iron). Spectra were collected at 52.05 MHz with a pulse duration of 5 μs (90°) and relaxation time of 2 s. Higher iron contents in these two samples enabled a faster relaxation time to be used than with the M–S–H materials. Chemical shifts were externally referenced to either MgO (26 ppm) or a 1 M $MgCl_2$ (0 ppm) solution.

# 3. Results and discussion

## 3.1 Influence of $(NaPO_3)_6$ addition

**3.1.1. Mini-slump.** The addition of $(NaPO_3)_6$ as an inorganic dispersant led to vast differences in the workability between the samples produced, as shown in Fig. 1. With no phosphate addition, the paste was thick and lacked fluidity, and a w/b ratio as high as 1.6 was required to achieve a mini-slump of ~80 $cm^2$. For comparison, using a mini-slump test in this geometry, a typical Portland cement paste with a w/b ratio of 0.36 and no organic admixtures achieved 27 $cm^2$, and with a w/b ratio of 0.5 achieved 68 $cm^2$.[22]

The addition of 1 wt% $Na(PO_3)_6$ consistently produced a higher fluidity than the other formulations, though only marginally more than the 2 wt% formulation. Both 1 and 2 wt% enabled retention of a high fluidity, ~130 $cm^2$, down to w/b = 0.7, with zero slump only reached at w/b = 0.50 using 1 wt% $Na(PO_3)_6$, and w/b = 0.55 using 2 wt%. Some loss of fluidity was observed at 5 wt% $(NaPO_3)_6$ addition, with higher w/b ratios required in order to achieve similar mini-slump values compared to the formulations with 1 and 2 wt% $(NaPO_3)_6$. This indicates that a threshold limit exists, beyond which the dispersion is no longer as effective, when too much phosphate is added.

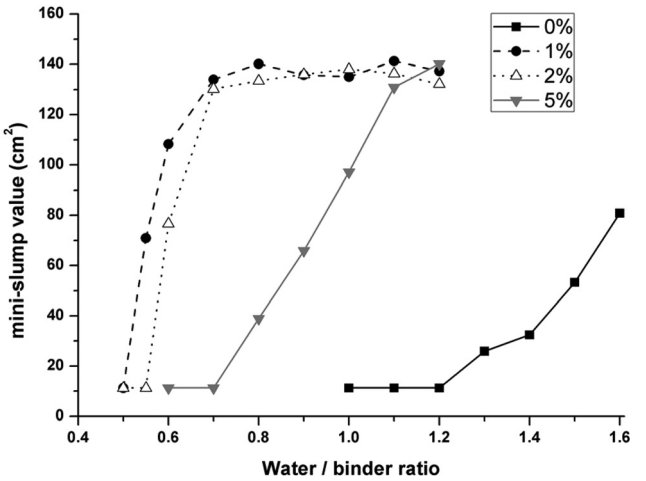


**Fig. 1** Mini-slump values for 1 : 1 $Mg(OH)_2 : SiO_2$ with 0–5 wt% $(NaPO_3)_6$ as shown in the legend, as a function of water/binder ratio. A measurement of 11.3 $cm^2$ indicates no slump, as this is the initial slump cone area.

The ability to maintain a high workability over a wide range of w/b ratios by using $(NaPO_3)_6$ as a dispersant enables a wider range of sludges to be used as a feedstock, due to their variable water content. Correspondingly, significantly less water is required to fluidise the system, compared to the phosphate free system. This is important, as the w/b ratio has a key impact on porosity in cementitious systems, and reducing water content is the most straightforward way to lower the porosity of the hardened material. Porosity of a cementitious binder is intrinsically linked to permeability, and consequently plays a major role in determining the mobility of radionuclides in the long-term leaching of cementitious wasteforms.[24]

**3.1.2. Compressive strength.** In the hardened state, the physical effects of changing the dose of $(NaPO_3)_6$ had only minor effects for a given w/b ratio. Fig. 2 shows the development of compressive strength as a function of curing duration for samples with a w/b ratio of 1.0. All samples exhibited slow strength gain during the first 28 days, with the samples containing any amount of $(NaPO_3)_6$ producing similar compressive strengths at each age of curing. The low strengths shown here are related to the high water/binder ratio of this sample set, which prevents the development of a strong microstructure. The sample formed in the absence of $(NaPO_3)_6$ produced the lowest strength after 28 days. This is likely to be a consequence of the presence of voids and bubbles within the samples caused by the extremely viscous paste produced, which was difficult to cast into the moulds despite the use of a vibrating table.

 

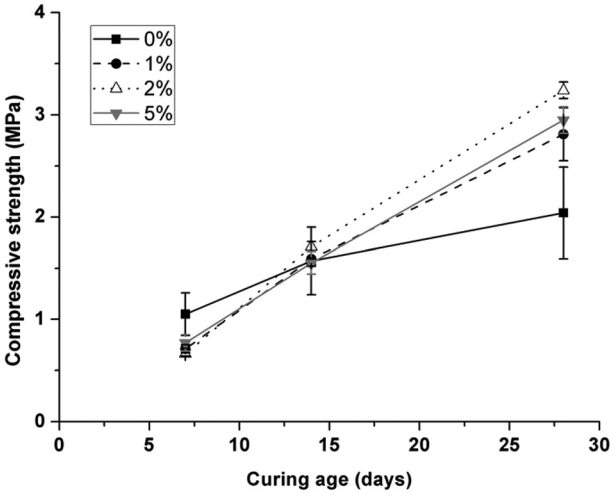


Fig. 2 Compressive strength of 1 : 1 $Mg(OH)_2 : SiO_2$ pastes, w/b = 1.0, with 0–5 wt% $(NaPO_3)_6$.

All of the samples produced with w/b = 1.0 exhibited lower compressive strengths than is recommended for use in a typical nuclear waste package (4 MPa for a 500 L drum),[25] but at 14 and 28 days did exceed the 0.7 MPa which is the baseline performance requirement for material handling. On this basis, and to offer chemical consistency throughout all samples, this w/b ratio was selected for use in characterisation of the hardened binder products.

**3.1.2. X-ray diffraction.** Fig. 3 shows similar hydration products formed in the tested samples, with brucite ($Mg(OH)_2$, PDF # 74-2220) and silica fume consumed to varying degrees at different levels of phosphate addition, to produce M–S–H. Calcite ($CaCO_3$, PDF # 05-0586) was identified as a minor impurity in the commercial-grade $Mg(OH)_2$. In the XRD patterns poorly crystalline M–S–H is clearly observed *via* diffuse scattering at 20°, 36° and 61° 2$\theta$, with a minor diffuse reflection at 28° 2$\theta$. These diffractograms are similar to those observed for other M–S–H systems,[13b,15b] as well as for mechanically amorphised talcs[26] and for ground chrysotile; these phases are both considered potential structural models for M–S–H.[27] Excess silica fume is identified *via* a diffuse reflection centred at 20° 2$\theta$, partially overlapping one of the M–S–H reflections. The formation of M–S–H appeared to be retarded when $(NaPO_3)_6$ was added beyond 1 wt%; this was clearly observed in the XRD data for the 2 wt% and 5 wt% samples after 28 days of curing.

**3.1.3. Thermal analysis.** The derivative thermogravimetry (DTG) data presented in Fig. 4 correlate well with the diffractograms in Fig. 3, recording higher residual contents of $Mg(OH)_2$ (decomposition peak at ~400 °C[28]) in the samples with increasing addition of phosphate. The weight loss at temperatures up to ~150 °C is assigned to the release of adsorbed water from the surface of the M–S–H,[13c] as well as free water held in the pores of the hardened gel. Any crystalline talc present would lose structural water at 875–1000 °C,[28] and thus is identifiably absent from these samples (consistent with the XRD data), while poorly crystalline talcs, ground chrysotile, ground antigorite and M–S–H are known to lose water slowly over a wide temperature range below 700 °C.[13b,c,14b,27,29]

Table 1 shows a quantitative breakdown of the thermogravimetric data in key temperature regions of interest, for samples cured for different durations. The mass loss between 340–440 °C represents the quantity of unreacted $Mg(OH)_2$, and it is evident that even at 1 wt% addition of $(NaPO_3)_6$, the rate of $Mg(OH)_2$ consumption was reduced compared to the phosphate-free sample. More unreacted $Mg(OH)_2$ was present after 7 and 14 days of curing in the presence of phosphate, although for 1 and 2 wt% $(NaPO_3)_6$, parity with the phosphate-free system was reached after 28 days. Addition of 5 wt% phosphate

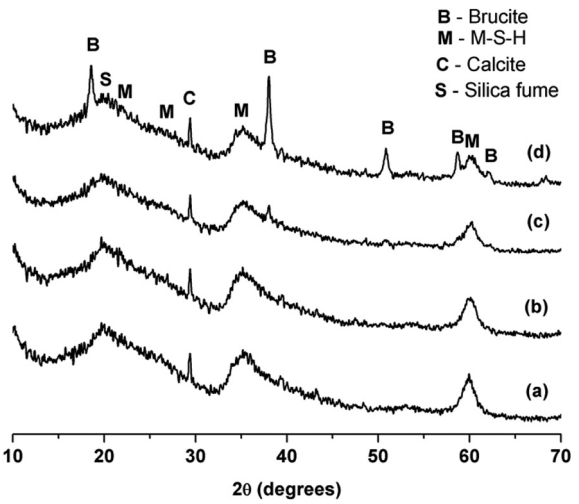


Fig. 3 X-ray diffraction patterns of 28 day-cured 1 : 1 $Mg(OH)_2 : SiO_2$ (w/b = 1.0) binders, with (a) 0, (b) 1, (c) 2 and (d) 5 wt% $(NaPO_3)_6$ addition.

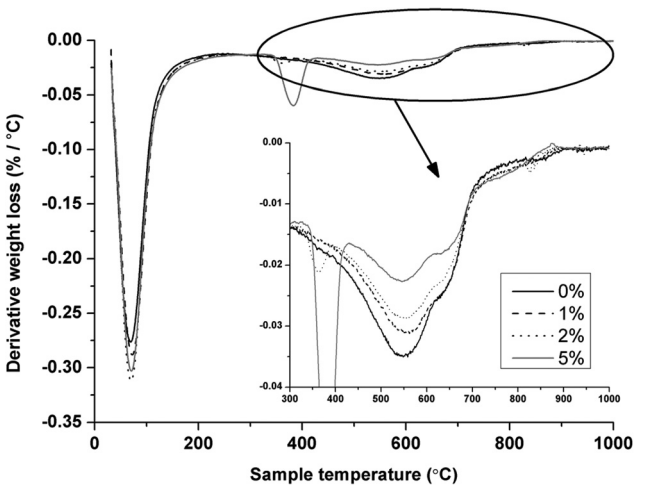


Fig. 4 DTG data for 1 : 1 $Mg(OH)_2 : SiO_2$ (w/b = 1.0) with 0–5 wt% $(NaPO_3)_6$, samples cured for 28 days. Inset shows the data above 300 °C with an expanded vertical scale.

Table 1 Mass loss (%) determined by TGA in different temperature ranges for 1 : 1 $Mg(OH)_2 : SiO_2$ (w/b = 1.0) with 0–5 wt% $(NaPO_3)_6$, at different curing durations. Uncertainty in calculated mass loss approx. ± 0.2%

| Mass loss (%) | | | | |
|---|---|---|---|---|
| | | Curing duration (days) | | |
| Temperature range (°C) | $Na(PO_3)_6$ (wt%) | 7 | 14 | 28 |
| 25 to 1000 | 0 | 27.2 | 27.9 | 29.2 |
| | 1 | 27.2 | 28.0 | 29.8 |
| | 2 | 26.1 | 27.4 | 30.1 |
| | 5 | 26.0 | 27.2 | 30.2 |
| 340 to 440 | 0 | 7.2 | 3.6 | 2.3 |
| | 1 | 10.2 | 5.5 | 2.2 |
| | 2 | 11.1 | 6.6 | 2.3 |
| | 5 | 10.6 | 7.6 | 4.1 |
| 450 to 1000 | 0 | 5.8 | 7.0 | 7.4 |
| | 1 | 5.4 | 6.2 | 7.0 |
| | 2 | 4.9 | 5.8 | 6.5 |
| | 5 | 4.2 | 4.8 | 5.4 |

reduces $Mg(OH)_2$ consumption at all ages studied, which is consistent with the XRD analysis in section 3.1.2; the mass loss peak is much more prominent in this sample than in the others shown in Fig. 4.

In Fig. 4, the region between 450 and 700 °C was seen to consist of two peaks, located at 550 °C and 640 °C. The peak at 550 °C is identified as being due specifically to M–S–H decomposition, with the peak at 640 °C assigned to the decomposition of calcite ($CaCO_3$),[30] which is introduced into each sample in equal proportions as an impurity in the $Mg(OH)_2$. As previously mentioned, the M–S–H loses water slowly and over a very wide temperature range, and thus, the mass loss event at 450–1000 °C is treated as characteristic for its analysis in Table 1, assuming a constant $CaCO_3$ contribution in all samples.

Magnesite ($MgCO_3$) decomposes at 527–615 °C,[30,31] but this phase was not identified by FTIR or XRD analysis, and so is not considered to contribute significantly to the DTG profile. Other (hydrous) magnesium carbonates would show distinctive low-temperature decomposition peaks, and also were not identified by XRD or FTIR.

The inset in Fig. 4 demonstrates a clear difference between the samples at 28 days of age, which is also quantified in Table 1 for each curing age. If it was assumed that M–S–H was structurally similar between the samples, this would indicate that M–S–H formation increased with curing age, and was retarded by the phosphate additions. This is in agreement with the differences observed in the diffraction patterns (Fig. 3). However, when comparing between the 0 and 1 wt% $(NaPO_3)_6$ data, the mass loss in Table 1, for $Mg(OH)_2$ decomposition (340–440 °C) remains the same (and XRD analysis (Fig. 4) suggests complete $Mg(OH)_2$ consumption), however the mass loss for M–S–H is different between these two. This suggests there might be a structural difference in the M–S–H gels forming due to the effect of the phosphate additive.

### 3.2. Structural evolution

**3.2.1. X-ray diffraction and thermal analysis.** Based on the discussion in the preceding section, further analysis was undertaken to understand the structural evolution of a phosphate modified system. A 1 : 1 $Mg(OH)_2 : SiO_2$ blend, using a w/b ratio of 1.0 and 2 wt% $(NaPO_3)_6$, was used as it developed the highest compressive strength among the samples tested at this w/b ratio.

The structural development of the binder can be seen in the diffractograms in Fig. 5, where decreasing intensity of the brucite ($Mg(OH)_2$) reflections is evident, along with increasing intensity of M–S–H reflections as the curing process progresses. This correlates well with the DTG data for samples with different curing durations (Fig. 6), demonstrating that longer-term curing led to lower mass loss at ~400 °C ($Mg(OH)_2$ decomposition), and larger mass losses in the regions 25–150 °C and ~550 °C, both of which can be used as indicators of M–S–H formation. As in Fig. 4, these DTG data also show a double peak in the region 450–700 °C. At early ages both peaks appear to have a similar intensity, but the peak at 550 °C increases at later curing ages, while that for the calcite decomposition at 650 °C remains constant.

The DTA data for the M–S–H binder (Fig. 7) show endothermic heat flow features in similar temperature ranges to those observed as mass loss peaks in DTG, but with an additional exotherm at 800–850 °C, which becomes sharper and more intense with greater sample maturity. This signal changes from two shallow exotherms (826 and 853 °C) after 7 days, to one strong sharp exotherm at 833 °C after 28 days. This change is not associated with a mass loss event in the DTG data, and therefore has been identified as the crystallisation of M–S–H.[13b,14b] Similar crystallisation events have been observed in thermal treatment of amorphised talc,[29a] which is converted to enstatite ($MgSiO_3$) at this temperature.[26] Comparable exotherms are noted in natural serpentine minerals, with chryso-

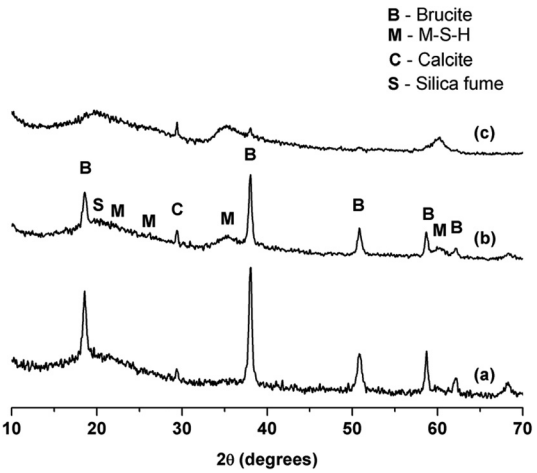


Fig. 5 X-ray diffractograms of 1 : 1 $Mg(OH)_2 : SiO_2$ (w/b = 1.0) with 2 wt% $(NaPO_3)_6$ at curing ages of (a) 7, (b) 14 and (c) 28 days.

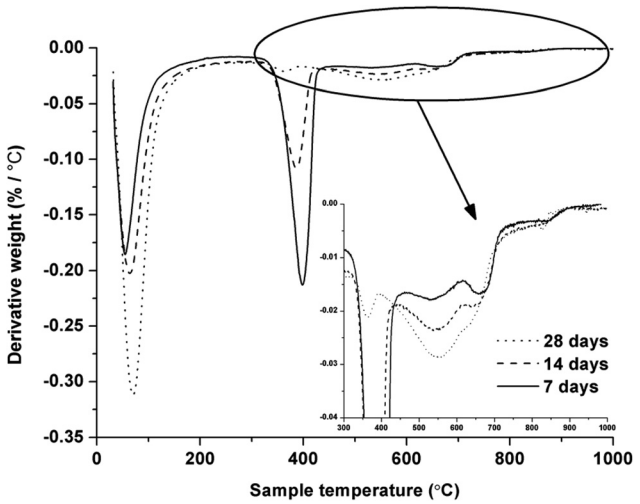


Fig. 6 DTG data for 1 : 1 $Mg(OH)_2 : SiO_2$ (w/b = 1.0) with 2 wt% $(NaPO_3)_6$, at curing ages of 7, 14 and 28 days.

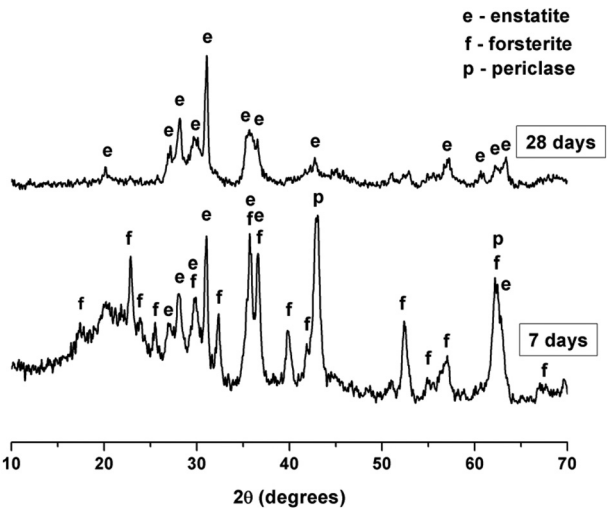


Fig. 8 XRD patterns of 1 : 1 $Mg(OH)_2 : SiO_2$ (w/b = 1.0) heated to 900 °C after 7 and 28 days of curing.

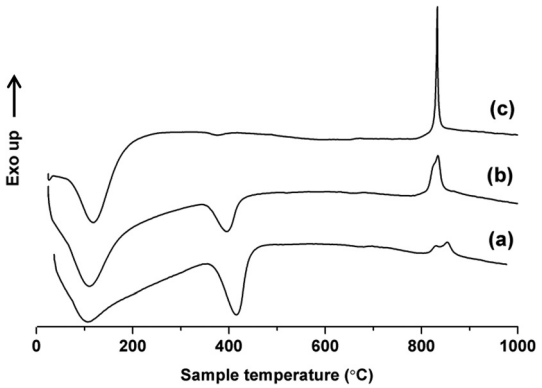


Fig. 7 DTA data for 1 : 1 $Mg(OH)_2 : SiO_2$ (w/b = 1.0) with 2 wt% $(NaPO_3)_6$, at curing ages of (a) 7, (b) 14 and (c) 28 days.

tile exhibiting a particularly sharp exotherm, forming a mixture of enstatite and forsterite ($Mg_2SiO_4$) upon heating.[32]

To further understand the exotherms observed in the DTA data, samples cured for 7 and 28 days were heated to 900 °C and analysed by XRD to determine the crystalline phases formed (Fig. 8). There is a clear difference observed between the samples. For the 28 day cured sample, only enstatite ($MgSiO_3$, PDF # 73-1758) was present, similar to the thermal treatment of amorphised talc as noted above. On the other hand, for the 7 day cured sample, in addition to enstatite, forsterite ($Mg_2SiO_4$, PDF # 34-189), periclase (MgO, PDF # 89-4248) and a broad band around ~22° 2$\theta$ assigned to low-crystallinity silica were also observed.

The presence of a single, sharp exotherm in the DTA data for the 28 day cured M–S–H (Fig. 7) can be explained by the presence of only enstatite after heating (Fig. 8). The shallower double peak observed in the DTA data for the 7 day cured sample could be attributed to a less developed and less homogeneous M–S–H gel structure, which crystallised into enstatite and forsterite at slightly different temperatures. The significant amount of periclase in the 7 day cured sample is due to the dehydroxylation of remnant $Mg(OH)_2$ upon heating.

**3.2.2. Fourier transform infrared spectroscopy.** The FTIR data shown in Fig. 9 demonstrate the evolution of phases with time, from the raw materials to the 28 day cured sample. The silica fume used in the present study (Fig. 9a) had a spectrum similar to that of vitreous silica, with broad bands at 1110 $cm^{-1}$ and 803 $cm^{-1}$ arising from Si–O stretching, and at 475 $cm^{-1}$ arising from O–Si–O bending.[33] $Mg(OH)_2$ (Fig. 9b) displayed a characteristic OH vibration at 3698 $cm^{-1}$ and libration at 415 $cm^{-1}$, with adsorbed water at ~3400 $cm^{-1}$ and the broad carbonate vibration of the calcite impurity at

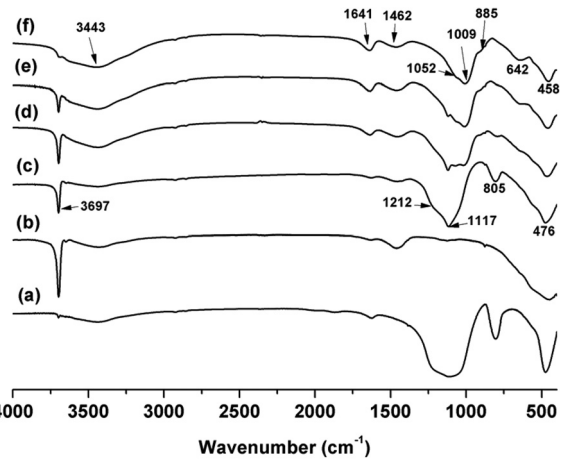


Fig. 9 FTIR spectra of (a) silica fume, (b) $Mg(OH)_2$, (c) 1 : 1 $Mg(OH)_2 : SiO_2$ with 2 wt% $(NaPO_3)_6$ as an anhydrous powder mix, and hydrated samples cured for (d) 7, (e) 14 and (f) 28 days (w/b = 1.0 for all hydrated samples).

1450 $cm^{-1}$.[34] The anhydrous mix (Fig. 9c) naturally showed the features of these raw materials combined.

Upon reaction, some of these features from the raw materials became less prominent (Fig. 9d, e), and the spectrum of the 28 day sample (Fig. 9f) became very similar to those previously reported for other M–S–H gels.[14a]

It is noted that the spectrum of the 28 day curing sample also resembles those of partially amorphised talc,[26,29a] ground chrysotile,[27] and ground antigorite.[29b] Libration of the $Mg_3OH$ unit in talc has been observed at 669 $cm^{-1}$, along with a vibration of chrysotile at 608 $cm^{-1}$ (shoulder at 645 $cm^{-1}$),[35] and similar modes are likely to be causing the peak seen in the M–S–H at 642 $cm^{-1}$. The Si–O–Si vibrations of the tetrahedral sheets within the talc structure are recorded at 1018 $cm^{-1}$ and 1047 $cm^{-1}$,[36] while amorphised chrysotile exhibits in-plane Si–O and out-of-plane Si–O stretching at 1025 $cm^{-1}$ and 1082 $cm^{-1}$ respectively, with asymmetric Si–O stretching at 960 $cm^{-1}$.[27] The broad band centred at 1009 $cm^{-1}$, with a broad shoulder at 1052 $cm^{-1}$, in the M–S–H is likely to be related to similar structural motifs.

The broad bands at ~3400 $cm^{-1}$ and 1640 $cm^{-1}$, which increase in intensity with age, are suggestive of water adsorbed to surfaces or incorporated in disordered reaction products. Some contribution in this region may also be from Si–OH vibrations due to the hydrated residual silica, which may also be producing the shoulder seen at ~885 $cm^{-1}$.

### 3.3. Nuclear magnetic resonance (NMR) spectroscopy

$^{29}Si$ and $^{25}Mg$ MAS NMR experiments were carried out to identify any structural changes occurring in these binders at advanced times of curing (up to 8 months), and the effect of $(NaPO_3)_6$ addition on the structure of the M–S–H formed in the 1 : 1 $Mg(OH)_2 : SiO_2$ binder system. The $^{29}Si$ NMR spectra of M–S–H samples with 0% and 2% $(NaPO_3)_6$ after 1 and 8 months of curing are reported in Fig. 10.

The $^{29}Si$ MAS NMR spectra in Fig. 10 are in good agreement with previously reported spectra for synthetic M–S–H type gels produced using MgO as the main Mg source.[14b,15a,37] Both the 1 and 8 month data sets resemble most closely the aged (6 months) high-Mg samples produced at 85 °C by Brew and Glasser,[14a] and the peak assignments presented here follow the general trends identified by those authors.

Deconvolution of the spectra enabled the identification of five peaks, with very minor shifts between spectra (Table 2). For the two spectra obtained after 1 month of curing, $Q^1$ and $Q^2$ peaks centred at around −81 and −86 ppm respectively were identified, with the $Q^3$ region split between two peaks centred at (a) −93 and (b) −97.7 ppm, respectively. It is noted

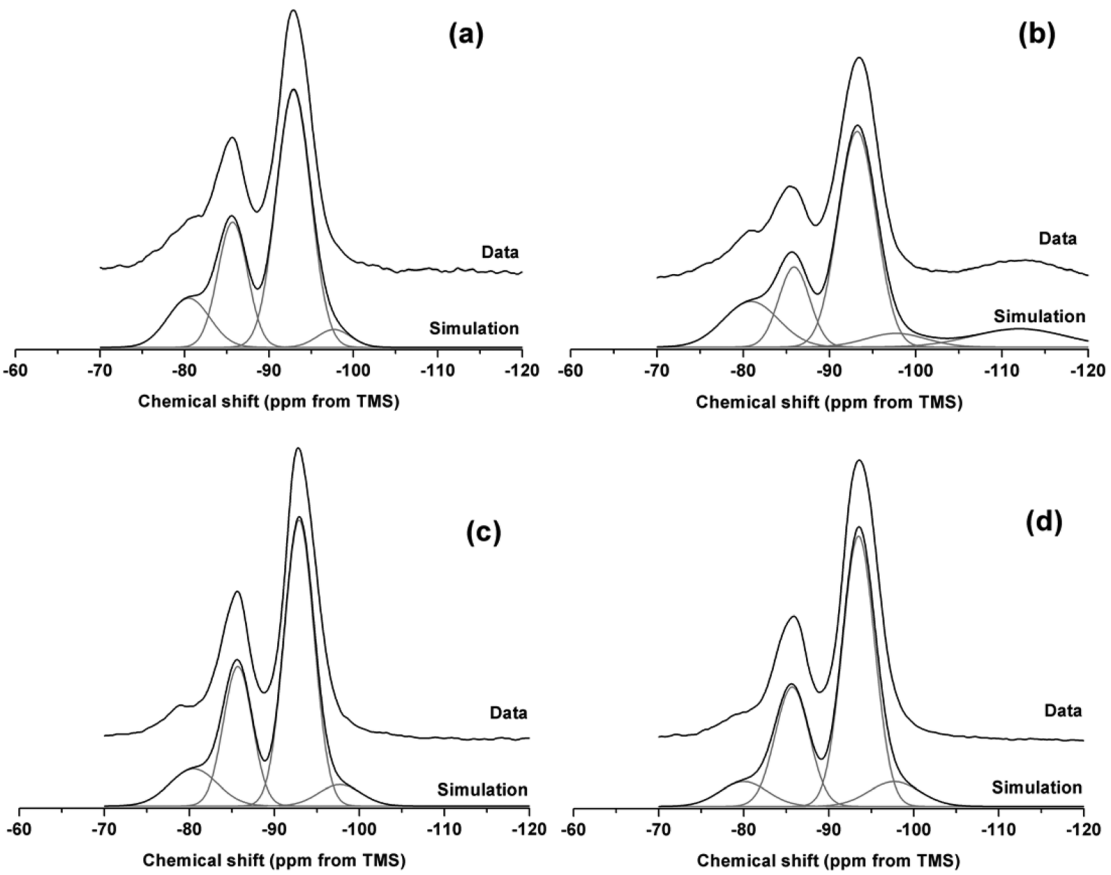


Fig. 10 $^{29}Si$ MAS NMR spectra for 1 : 1 $Mg(OH)_2 : SiO_2$ (w/b 1.0) with (a) 0 and (b) 2 wt% $(NaPO_3)_6$ at a curing age of 1 month, (c) 0 and (d) 2 wt% $(NaPO_3)_6$ after 8 months of curing. The data presented include a simulation and constituent peaks underneath.

 

Table 2 Peak positions and widths (ppm) for deconvolutions shown in Fig. 10. Estimated uncertainty in calculated intensities ± 1%

| | | 1 month | | | | | 8 months | | | |
|---|---|---|---|---|---|---|---|---|---|---|
| $(NaPO_3)_6$ | | $Q^1$ | $Q^2$ | $Q^3$(a) | $Q^3$(b) | $Q^4$ | $Q^1$ | $Q^2$ | $Q^3$(a) | $Q^3$(b) |
| 0 wt% | Centre | −80.5 | −85.7 | −92.9 | −97.7 | — | −80.5 | −85.7 | −92.9 | −97.7 |
| | FWHM | 5.9 | 4.1 | 4.8 | 4.7 | — | 6.6 | 4.0 | 4.1 | 5.9 |
| | Intensity (%) | 13.7 | 24.4 | 57.9 | 4.0 | — | 11.6 | 26.5 | 55.9 | 6.0 |
| 2 wt% | Centre | −80.9 | −85.9 | −93.2 | −97.7 | −112 | −80.0 | −85.7 | −93.5 | −97.7 |
| | FWHM | 7.5 | 4.2 | 5.2 | 8.2 | 12.7 | 6.6 | 4.7 | 4.5 | 7.1 |
| | Intensity (%) | 16.1 | 15.8 | 52.1 | 5.3 | 10.7 | 7.7 | 26.6 | 57.3 | 8.3 |

that the $^{29}$Si MAS NMR spectra of serpentine minerals and talc typically exhibit peaks in the $Q^3$ region, while broader $Q^1$ and $Q^2$ bands signify a less structured gel The major $Q^3$(a) peak at −93 ppm was consistent with the $Q^3$ resonance typically identified in both chrysotile[38] and antigorite,[39] while the smaller $Q^3$(b) peak at −97.7 ppm was assigned to a $Q^3$ site environment similar to those typically present in talc.[28]

The relatively high $Q^3$(a + b)/$Q^2$ intensity ratio in Fig. 10 is indicative of a high level of structural development in the gel. The addition of 2 wt% $(NaPO_3)_6$ leads to the presence of a peak centred at −112 ppm after 1 month, attributed to $Q^4$ species in unreacted silica fume[40] and indicating a lower extent of reaction, resulting in lower intensity $Q^3$ and $Q^2$ peaks. This indicates that with no addition of $(NaPO_3)_6$ the silica fume had completely reacted, while the presence of phosphate had retarded the conversion of silica fume to M–S–H.

After 8 months of curing, the spectra had changed slightly compared with those observed in the specimens after 1 month of curing. There was a decrease in the $Q^1$ region for both 0 and 2 wt% phosphate samples, which suggests that further structural development of M–S–H occurred in the samples, leading towards the formation of a more cross-linked structure. After 8 months of curing the resonance assigned to the $Q^4$ sites of unreacted silica fume was no longer present in the phosphate-containing sample, indicating that the silica fume in these binders has been fully consumed at this time.

The structure of M–S–H has previously been proposed to resemble a poorly crystalline talc-like material.[13a] Talc typically exhibits a single $^{29}$Si peak at −97.7 ppm,[28] however this peak was only a minor $Q^3$ component within the binders produced in this study. The major $Q^3$ component was identified at −93 ppm, which corresponds to that typically found in the serpentine group of minerals (polymorphs of $Mg_3(Si_2O_5)(OH)_4$, such as chrysotile, lizardite and antigorite). The reported $^{29}$Si NMR peak locations for these minerals vary slightly from publication to publication, potentially due to the slight variations in chemical composition of each natural sample due to Fe, Ca and Al inclusions. Both chrysotile[38] and antigorite[39b] have reported values close to −93 ppm, although the antigorite spectrum is broad, while data for lizardite are difficult to obtain.

To clarify the details of the M–S–H structure formed here, natural mineral samples of lizardite and antigorite were obtained and analysed *via* $^{29}$Si and $^{25}$Mg MAS NMR. These samples contained traces of iron (7.0 wt% in antigorite, 3.4 wt% in lizardite, on an oxide basis as determined by X-ray fluorescence), broadening the signal and affecting the relaxation times. This was more severe for the antigorite sample. The lizardite was also slightly aluminous (7.1 wt% $Al_2O_3$), as Al often substitutes for Si in natural samples.[41] These spectra are shown in Fig. 11, both exhibiting strong signals within the $Q^3$ region at around −90 ppm. The broad antigorite spectral feature at −87.8 ppm is downfield of the principal $Q^3$ peaks in

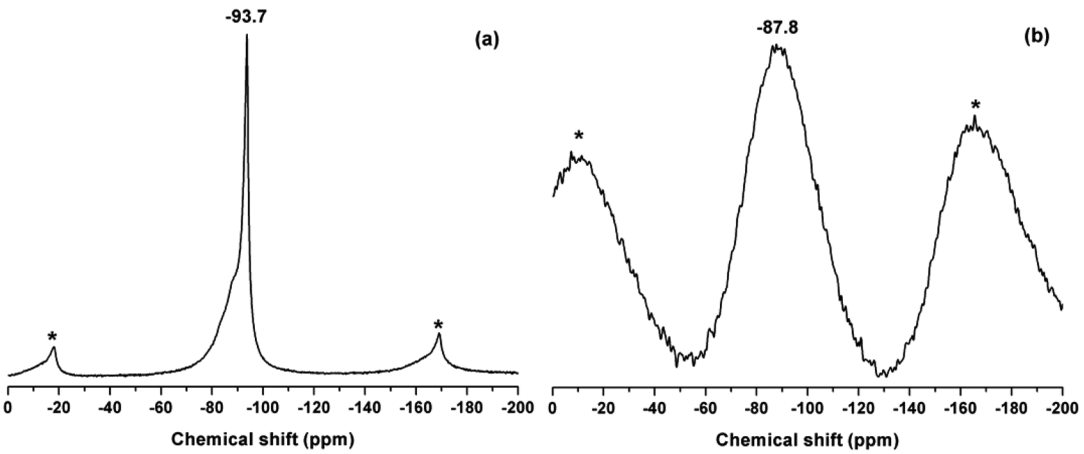


Fig. 11 $^{29}$Si MAS NMR spectra for: (a) lizardite, (b) antigorite. Spinning sidebands marked with *.

the M–S–H, although the spectrum is not of high resolution, whereas the main lizardite peak at −93.7 ppm matches very closely to the $Q^3$(a) site observed within the M–S–H samples. There does exist a broad feature downfield of this peak, which significantly reduces in area when cross polarised with $^1$H, suggesting that these environments may resemble less ordered, less hydrated lizardite-like assemblages than the primary $Q^3$(a) site.

$^{25}$Mg MAS NMR data are significantly more difficult to obtain and interpret than is the case for $^{29}$Si. The low natural abundance (10%) and low resonance frequency of $^{25}$Mg often necessitate the use of very high field instruments (*e.g.* 20 T used here).[42] Combined with its quadrupolar nature (spin $^5/_2$), this makes the interpretation of spectra complex, although recent advances in this field are shedding more light on this less well studied nucleus.[42,43]

$^{25}$Mg MAS NMR spectra of lizardite, antigorite and talc are overlaid with the spectra of 1 and 8 month cured M–S–H samples (with 0% $(Na_3PO_4)_6$) in Fig. 12. A clear change in line-shape is observed in the M–S–H samples as curing progresses, with the spectrum shifting upfield. The 8 month M–S–H sample specifically aligns well with the lizardite spectrum (as compared in Fig. 13), compared to the antigorite or talc spectra. It should be noted that being a natural sample, the lizardite contains an impurity of ~12 wt% $Mg(OH)_2$, which will modify the $^{25}$Mg spectrum. At this field strength, second-order quadrupolar interactions of the central transition cause $Mg(OH)_2$ to exhibit a split double peak from its single Mg site.[44] This double peak is centred −9 ppm, which is in the central part of the lizardite spectrum. Though contributing to the peak, this is unlikely to significantly alter the peak position.

Studies of mineral formation in the M–S–H system have evolved significantly over time, as thermodynamic and kinetic data are refined. Previous papers have included chrysotile as a stable phase, or exclude lizardite from calculations, leading to predictions that either antigorite or chrysotile are stable at low temperatures.[45] Recently, however, it has been concluded that lizardite is the stable phase in the M–S–H system below ~300 °C, with antigorite only stable at temperatures exceeding 250 °C.[46] Chrysotile is postulated to only form from supersaturated solutions as a kinetic effect,[47] having no thermodynamically stable range within the M–S–H field.[46] Given this assessment, it seems reasonable to conclude that the serpentine-like feature in the M–S–H gel is likely to be structurally similar to the thermodynamically most stable phase; this is lizardite, given the formation conditions.

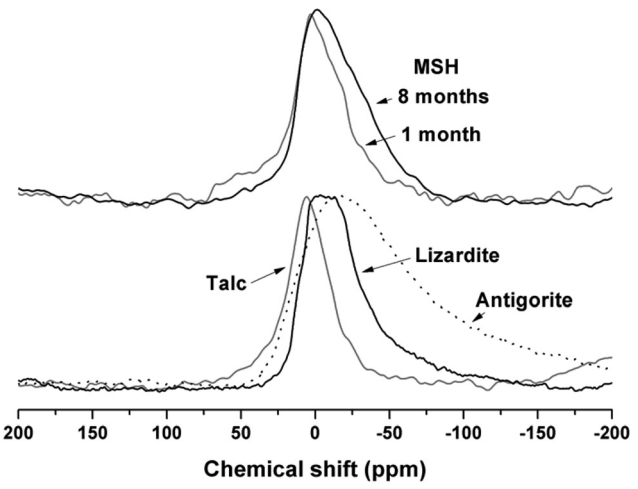


Fig. 12 $^{25}$Mg MAS NMR spectra of 1 and 8 month cured M–S–H with reference materials. Note that the antigorite spin rate was increased from 10 to 14 kHz due to line broadening from iron.

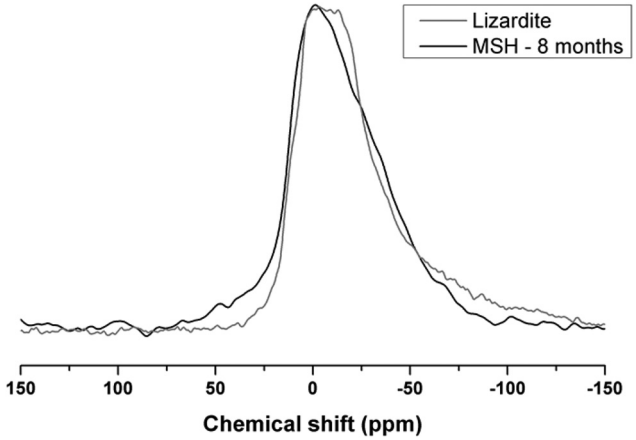


Fig. 13 $^{25}$Mg MAS NMR spectra of 8 month cured M–S–H, and comparison with lizardite.

This assignment fits well with the chemistry of the binders produced within the $Mg(OH)_2$–$SiO_2$–$H_2O$ system studied; assuming complete reaction of $Mg(OH)_2$ and $SiO_2$ in these samples, the molar Mg/Si ratio of this binder should be ~0.95. This ratio is between those of talc (0.75) and lizardite (1.5), and thus suggests that the structural motifs of both mineral types are likely to be present in the gel structure. It does, however, appear that ageing of the gels produces a gel which is closer in structure to lizardite than talc, as evidenced by the aforementioned NMR data.

Analysis of M–S–H gels at different Mg/Si ratios by Brew and Glasser[14a] showed that increasing the Mg/Si ratio of the M–S–H gel induced changes in the peak positions of the $^{29}$Si MAS NMR resonances towards less negative chemical shift values. In that study, aged M–S–H gels formulated with Mg/Si ratios of 0.82 and 0.89 exhibited $Q^3$ bands at chemical shifts of −98.8 ppm and −97.7 ppm respectively, whereas M–S–H gels produced with an Mg/Si ratio of 0.94 showed a peak shifted to −94.6 ppm. The authors noted that their FTIR and $^{29}$Si NMR data more closely resembled chrysotile than talc. This suggests that there is a shift from the formation of a poorly crystalline talc-like structure to a poorly crystalline serpentine-like material when the Mg/Si ratio is increased. It is important to understand this structural shift as a function of composition, as knowledge of the structure of the M–S–H can help to predict its future behaviour, likely stability, and the quantity of

 

$Mg(OH)_2$ which can be accommodated into this system, and this is central to its use as a nuclear wasteform. The addition of phosphate to enhance fluidity does not appear to significantly alter the final M–S–H structure, although it retards the kinetics of conversion of amorphous silica to M–S–H in the first month of curing.

## 4. Conclusions

$Mg(OH)_2$ has been successfully used to produce an M–S–H cement. The M–S–H produced was similar to high-Mg gels described in other works, and largely consists of a poorly crystalline serpentine-like assembly, which we have assigned as a lizardite-type structure. The addition of $(NaPO_3)_6$ was effective in dispersing the $Mg(OH)_2$ particles and adding fluidity to the system. Higher doses of phosphate (2 wt% or more) delay the formation of M–S–H, with 1 wt% addition conferring the highest fluidity with minimal impact on M–S–H formation. The developments presented in this work will enable M–S–H to be used as an encapsulant for both low and high-water content sludges without the occurrence of bleed water, which would otherwise need to be decanted and treated as a secondary waste stream if Portland cement-based grouts were used to treat these sludges. The implementation of these cements for Magnox sludge encapsulation is, however, likely to be hindered by slow strength development in samples with a high water/binder ratio, despite providing an effective method of converting this waste into a cementitious binder. Application of this cement would also be highly dependent on the Mg/Si ratio in the resultant cementitious slurry. Retrieved sludges can vary widely in their $Mg(OH)_2$ contents. This study has highlighted the potential for control of gel nanostructure depending on the Mg/Si ratio.

## Acknowledgements

This study has been sponsored by the Engineering and Physical Sciences Research Council through the University of Sheffield/University of Manchester Doctoral Training Centre 'Nuclear FiRST' and through a Nuclear Decommissioning Authority CASE award, under supervision by the National Nuclear Laboratory. The donation of microsilica by ELKEM Silicon Material (United Kingdom) is greatly appreciated. Solid-state NMR spectra were obtained at the EPSRC UK National Solid-state NMR Service at Durham, and we are grateful for the assistance of Dr David Apperley related to the experiments conducted at that facility. The UK 850 MHz solid-state NMR Facility used in this research was funded by EPSRC and BBSRC, as well as the University of Warwick including *via* part funding through Birmingham Science City Advanced Materials Projects 1 and 2 supported by Advantage West Midlands (AWM) and the European Regional Development Fund (ERDF). The input of Dr Dinu Iuga in conducting experiments is also gratefully acknowledged.

## References

1 *Nuclear Decomissioning Authority Waste stream 2D95.1 Magnox fuel storage pond sludge*, NDA, 2013.
2 C. R. Gregson, D. T. Goddard, M. J. Sarsfield and R. J. Taylor, Combined electron microscopy and vibrational spectroscopy study of corroded Magnox sludge from a legacy spent nuclear fuel storage pond, *J. Nucl. Mater.*, 2011, **412**(1), 145–156.
3 S. Parry, F. Livens and L. O'Brien, Corroded Magnox sludge and plutonium waste cementation, *Geochim. Cosmochim. Acta*, 2007, **71**(15, Supplement), A747–A815.
4 *Nuclear Decomissioning Authority Waste stream 2D16: Magnox fuel storage pond sludge*, NDA, 2007.
5 M. Atkins and F. P. Glasser, Application of portland cement-based materials to radioactive waste immobilization, *Waste Manage.*, 1992, **12**(2–3), 105–131.
6 N. C. Collier and N. B. Milestone, The encapsulation of $Mg(OH)_2$ sludge in composite cement, *Cem. Concr. Res.*, 2010, **40**(3), 452–459.
7 T. Hough and S. Palethorpe, Development of a direct encapsulation technique for the treatment of a mixed sludge/solid waste, in *WM'07 Conference*, Tucson, AZ, 2007.
8 L. J. Vandeperre, M. Liska and A. Al-Tabbaa, Microstructures of reactive magnesia cement blends, *Cem. Concr. Compos.*, 2008, **30**(8), 706–714.
9 E. M. Gartner and D. E. Macphee, A physico-chemical basis for novel cementitious binders, *Cem. Concr. Res.*, 2011, **41**(7), 736–749.
10 A. D. Wilson and J. W. Nicholson, *Acid–base cements – Their biomedical and industrial applications*, Cambridge University Press, Cambridge, 1993.
11 B. Tooper and L. Cartz, Structure and formation of magnesium oxychloride Sorel cements, *Nature*, 1966, **211**, 64–66.
12 (*a*) T. Zhang, C. R. Cheeseman and L. J. Vandeperre, Development of low pH cement systems forming magnesium silicate hydrate (M–S–H), *Cem. Concr. Res.*, 2011, **41**(4), 439–442; (*b*) J. Szczerba, R. Prorok, E. Śnieżek, D. Madej and K. Maślona, Influence of time and temperature on ageing and phases synthesis in the $MgO–SiO_2–H_2O$ system, *Thermochim. Acta*, 2013, **567**, 57–64; (*c*) T. Zhang, L. J. Vandeperre and C. Cheeseman, Bottom-up design of a cement for nuclear waste encapsulation, in *Ceramic Materials for Energy Applications*, John Wiley & Sons, Inc., 2011, pp. 41–49.
13 (*a*) T. Mitsuda, Paragenesis of 11 Å tobermorite and poorly crystalline hydrated magnesium silicate, *Cem. Concr. Res.*, 1973, **3**(1), 71–80; (*b*) T. Mitsuda and H. Taguchi, Formation of magnesium silicate hydrate and its crystallization to talc, *Cem. Concr. Res.*, 1977, **7**(3), 223–230; (*c*) N. Takahashi, M. Tanaka, T. Satoh and T. Endo, Study of synthetic clay minerals. III. synthesis and characterization of two dimensional talc, *Bull. Chem. Soc. Jpn.*, 1994, **67**(9), 2463–2467.
14 (*a*) D. R. M. Brew and F. P. Glasser, Synthesis and characterisation of magnesium silicate hydrate gels, *Cem. Concr.*

*Res.*, 2005, **35**(1), 85–98; (*b*) J. Temuujin, K. Okada and K. J. D. MacKenzie, Formation of layered magnesium silicate during the aging of magnesium hydroxide–silica mixtures, *J. Am. Ceram. Soc.*, 1998, **81**(3), 754–756.

15 (*a*) J. Wei, Q. Yu, W. Zhang and H. Zhang, Reaction products of MgO and microsilica cementitious materials at different temperatures, *J. Wuhan Univ. Technol. Mater. Sci. Ed.*, 2011, **26**(4), 745–748; (*b*) J. Wei, Y. Chen and Y. Li, The reaction mechanism between MgO and microsilica at room temperature, *J. Wuhan Univ. Technol. Mater. Sci. Ed.*, 2006, **21**(2), 88–91.

16 (*a*) M. Santhanam, M. D. Cohen and J. Olek, Mechanism of sulfate attack: A fresh look: Part 1: Summary of experimental results, *Cem. Concr. Res.*, 2002, **32**(6), 915–921; (*b*) D. Bonen and M. D. Cohen, Magnesium sulfate attack on portland cement paste—II. Chemical and mineralogical analyses, *Cem. Concr. Res.*, 1992, **22**(4), 707–718.

17 D. R. M. Brew and F. P. Glasser, The magnesia-silica gel phase in slag cements: alkali (K, Cs) sorption potential of synthetic gels, *Cem. Concr. Res.*, 2005, **35**(1), 77–83.

18 C. L. Corkhill, N. J. Cassingham, P. G. Heath and N. C. Hyatt, Dissolution of UK high-level waste glass under simulated hyperalkaline conditions of a colocated geological disposal facility, *Int. J. Appl. Glass Sci.*, 2013, **4**(4), 341–356.

19 J. L. García Calvo, A. Hidalgo, C. Alonso and L. Fernández Luco, Development of low-pH cementitious materials for HLRW repositories: Resistance against ground waters aggression, *Cem. Concr. Res.*, 2010, **40**(8), 1290–1297.

20 (*a*) A. J. Young, P. Warwick, A. E. Milodowski and D. Read, Behaviour of radionuclides in the presence of superplasticiser, *Adv. Cem. Res.*, 2013, **25**(1), 32–43; (*b*) A. P. Clacher and M. M. Cowper, *Effect of ADVA cast 551 on the solubility of plutonium(IV) and uranium(VI); Serco Report SERCO/TAS/003145/001 to NDA RWMD*, Harwall, UK, 2011.

21 (*a*) S. Otroj, M. A. Bahrevar, F. Mostarzadeh and M. R. Nilforoshan, The effect of deflocculants on the self-flow characteristics of ultra low-cement castables in $Al_2O_3$–SiC–C system, *Ceram. Int.*, 2005, **31**(5), 647–653; (*b*) F. Andreola, E. Castellini, G. Lusvardi, L. Menabue and M. Romagnoli, Release of ions from kaolinite dispersed in deflocculant solutions, *Appl. Clay Sci.*, 2007, **36**(4), 271–278.

22 D. L. Kantro, Influence of water-reducing admixtures on properties of cement paste – a miniature slump test, *Cem., Concr. Aggr.*, 1980, **2**(2), 95–102.

23 W. S. Rasband, *ImageJ, 1.48*, U. S. National Institutes of Health, Bethesda, Maryland, 2014.

24 M. I. Ojovan and W. E. Lee, *An introduction to nuclear waste immobilisation*, Elsevier, Oxford, 2005.

25 NDA, *WPS/700: 500 litre drum waste package specifications: explanatory material and design guidelines*, Nuclear Decommissioning Authority, UK, 2008.

26 J. Liao and M. Senna, Thermal behavior of mechanically amorphized talc, *Thermochim. Acta*, 1992, **197**(2), 295–306.

27 H. Suquet, Effects of dry grinding and leaching on the crystal structure of chrysotile, *Clays Clay Miner.*, 1989, **37**(5), 439–445.

28 K. J. D. MacKenzie and R. H. Meinhold, The thermal reactions of talc studied by $^{29}$Si and $^{25}$Mg MAS NMR, *Thermochim. Acta*, 1994, **244**, 195–203.

29 (*a*) E. F. Aglietti, The effect of dry grinding on the structure of talc, *Appl. Clay Sci.*, 1994, **9**(2), 139–147; (*b*) A. Drief and F. Nieto, The effect of dry grinding on antigorite from Mulhacen, Spain, *Clays Clay Miner.*, 1999, **47**(4), 417–424.

30 W. Smykatz-Kloss, *Differential thermal analysis. Application and results in mineralogy*, Springer-Verlag, Berlin, 1974.

31 J. H. Sharp, F. W. Wilburn and R. M. McIntosh, The effect of procedural variables on TG, DTG and DTA curves of magnesite and dolomite, *J. Thermal Anal.*, 1991, **37**(9), 2021–2029.

32 C. Viti, Serpentine minerals discrimination by thermal analysis, *Am. Mineral.*, 2010, **95**(4), 631–638.

33 (*a*) E. R. Lippincott, A. V. Valkenburg, C. E. Weir and E. N. Bunting, Infrared studies on polymorphs of silicon dioxide and germanium dioxide, *J. Res. Natl. Bur. Stand.*, 1958, **61**(1), 61–70; (*b*) M. Ocaña, V. Fornés and C. J. Serna, The variability of the infrared powder spectrum of amorphous $SiO_2$, *J. Non-Cryst. Solids*, 1989, **107**(2–3), 187–192.

34 (*a*) Y. I. Ryskin, The vibrations of protons in minerals: hydroxyl, water and ammonium, in *The Infrared Spectra of Minerals*, ed. V. C. Farmer, Mineralogical Society, London, 1974, pp. 137–182; (*b*) N. Chukanov, *Infrared spectra of mineral species*, Springer, Netherlands, 2014, pp. 21–1701.

35 V. C. Farmer, The layer silicates, in *The infrared spectra of minerals*, ed. V. C. Farmer, Mineralogical Society, London, 1974, pp. 331–364.

36 J. D. Russell, V. C. Farmer and B. Velde, Replacement of OH by OD in layer silicates, and identification of the vibrations of these groups in infra-red spectra, *Mineral. Mag.*, 1970, **37**(292), 869–879.

37 J.-B. d'Espinose de la Caillerie, M. Kermarec and O. Clause, $^{29}$Si NMR observation of an amorphous magnesium silicate formed during impregnation of silica with Mg(II) in aqueous solution, *J. Phys. Chem.*, 1995, **99**(47), 17273–17281.

38 K. J. D. MacKenzie and R. H. Meinhold, Thermal reactions of chrysotile revisited: A $^{29}$Si and $^{25}$Mg MAS NMR study, *Am. Mineral.*, 1994, **79**, 43–50.

39 (*a*) K. Kosuge, K. Shimada and A. Tsunashima, Micropore formation by acid treatment of antigorite, *Chem. Mater.*, 1995, **7**(12), 2241–2246; (*b*) S. Nakata, S. Asaoka, T. Kondoh and H. Takahashi, Characterization of natural zeolites and clay minerals by high-resoultion solid-state NMR, *Nendo Kagaku*, 1986, **26**, 197–208.

40 H. Hilbig, F. H. Köhler and P. Schießl, Quantitative $^{29}$Si MAS NMR spectroscopy of cement and silica fume containing paramagnetic impurities, *Cem. Concr. Res.*, 2006, **36**(2), 326–329.

41 (*a*) M. Mellini, The crystal structure of lizardite 1T: hydrogen bonds and polytypism, *Am. Mineral.*, 1982, **67**, 587–598; (*b*) R. Trittschack and B. Grobéty, Dehydroxylation kinetics of lizardite, *Eur. J. Mineral.*, 2012, **24**(1), 47–57;

 

(*c*) L. J. Caruso and J. V. Chernosky, The stability of lizardite, *Can. Mineral.*, 1979, **17**(4), 757–769.

42 P. J. Pallister, I. L. Moudrakovski and J. A. Ripmeester, Mg-25 ultra-high field solid state NMR spectroscopy and first principles calculations of magnesium compounds, *Phys. Chem. Chem. Phys.*, 2009, **11**(48), 11487–11500.

43 (*a*) L. S. Cahill, J. V. Hanna, A. Wong, J. C. C. Freitas, J. R. Yates, R. K. Harris and M. E. Smith, Natural abundance $^{25}$Mg solid-state NMR of Mg oxyanion systems: A combined experimental and computational study, *Chem. – Eur. J.*, 2009, **15**(38), 9785–9798; (*b*) S. E. Ashbrook and S. Sneddon, New methods and applications in solid-state nmr spectroscopy of quadrupolar nuclei, *J. Am. Chem. Soc.*, 2014, **136**(44), 15440–15456; (*c*) D. Laurencin, C. Gervais, H. Stork, S. Krämer, D. Massiot and F. Fayon, $^{25}$Mg solid-state NMR of magnesium phosphates: high magnetic field experiments and density functional theory calculations, *J. Phys. Chem. C*, 2012, **116**(37), 19984–19995; (*d*) J. C. C. Freitas and M. E. Smith, Recent advances in solid-state 25Mg NMR spectroscopy, in *Annual Reports on NMR Spectroscopy*, ed. A. W. Graham, Academic Press, 2012, vol. 75, pp. 25–114.

44 C. P. Slichter, *Principles of magnetic resonance*, Springer-Verlag, Berlin, 3rd edn, 1996.

45 (*a*) D. S. O'Hanley and F. J. Wicks, Conditions of formation of lizardite, chrysotile and antigorite, Cassiar, British Columbia, *Can. Mineral.*, 1995, **33**, 753–773; (*b*) H. W. Day, J. V. Chernosky and H. J. Kumin, Equilibria in the system $MgO–SiO_2–H_2O$: a thermodynamic analysis, *Am. Mineral.*, 1985, **70**, 237–248.

46 B. W. Evans, The serpentinite multisystem revisited: chrysotile is metastable, *Int. Geol. Rev.*, 2004, **46**, 479–506.

47 (*a*) E. K. Peters, D-$^{18}$O enriched waters of the Coast Range Mountains, northern California: Connate and ore-forming fluids, *Geochim. Cosmochim. Acta*, 1993, **57**, 1093–1104; (*b*) H. W. Nesbitt and O. P. Bricker, Low temperature alteration process affecting ultramafic bodies, *Geochim. Cosmochim. Acta*, 1978, **42**, 403–409.